

Article

Remote Sensing Methodology for Roughness Estimation in Ungauged Streams for Different Hydraulic/Hydrodynamic Modeling Approaches

George Papaioannou ^{1,2}, Vassiliki Markogianni ¹, Athanasios Loukas ³ and Elias Dimitriou ^{1,*}

¹ Institute of Marine Biological Resources and Inland Waters, Hellenic Centre for Marine Research, 19013 Anavyssos, Greece; gpapaio@fmenr.duth.gr (G.P.); vmarkogianni@hcmr.gr (V.M.)

² Department of Forestry and Management of the Environment and Natural Resources, Democritus University of Thrace, 68200 Orestiada, Greece

³ School of Rural and Surveying Engineering, Aristotle University of Thessaloniki, 54124 Thessaloniki, Greece; agloukas@topo.auth.gr

* Correspondence: elias@hcmr.gr; Tel.: +30-2291076389

Abstract: This study investigates the generation of spatially distributed roughness coefficient maps based on image analysis and the extent to which those roughness coefficient values affect the flood inundation modeling using different hydraulic/hydrodynamic modeling approaches ungauged streams. Unmanned Aerial Vehicle (UAV) images were used for the generation of high-resolution Orthophoto mosaic (1.34 cm/px) and Digital Elevation Model (DEM). Among various pixel-based and object-based image analyses (OBIA), a Grey-Level Co-occurrence Matrix (GLCM) was eventually selected to examine several texture parameters. The combination of local entropy values (OBIA method) with Maximum Likelihood Classifier (MLC; pixel-based analysis) was highlighted as a satisfactory approach (65% accuracy) to determine dominant grain classes along a stream with inhomogeneous bed composition. Spatially distributed roughness coefficient maps were generated based on the riverbed image analysis (grain size classification), the size-frequency distributions of river bed materials derived from field works (grid sampling), detailed land use data, and the usage of several empirical formulas that used for the estimation of Manning's *n* values. One-dimensional (1D), two-dimensional (2D), and coupled (1D/2D) hydraulic modeling approaches were used for flood inundation modeling using specific Manning's *n* roughness coefficient map scenarios. The validation of the simulated flooded area was accomplished using historical flood extent data, the Critical Success Index (CSI), and CSI penalization. The methodology was applied and demonstrated at the ungauged Xerias stream reach, Greece, and indicated that it might be applied to other Mediterranean streams with similar characteristics and flow conditions.

Keywords: HEC-RAS; flood inundation modeling; modeling approach; spatial distributed roughness coefficient; UAV; remote sensing; image processing; image texture; river bed material mapping



Citation: Papaioannou, G.; Markogianni, V.; Loukas, A.; Dimitriou, E. Remote Sensing Methodology for Roughness Estimation in Ungauged Streams for Different Hydraulic/Hydrodynamic Modeling Approaches. *Water* **2022**, *14*, 1076. <https://doi.org/10.3390/w14071076>

Academic Editor: Bommanna Krishnappan

Received: 14 February 2022

Accepted: 26 March 2022

Published: 29 March 2022

Publisher's Note: MDPI stays neutral with regard to jurisdictional claims in published maps and institutional affiliations.



Copyright: © 2022 by the authors. Licensee MDPI, Basel, Switzerland. This article is an open access article distributed under the terms and conditions of the Creative Commons Attribution (CC BY) license (<https://creativecommons.org/licenses/by/4.0/>).

1. Introduction

Several fields of geomorphological research such as sediment transport and deposition [1–3], the study of flow resistance, and the prediction of flow velocities in open channel flow (e.g., [4,5]) can be described based on grain size measurements of fluvial sediments [6]. Many studies focused on methods for field measurements of riverbed sediment [7–10], including the pebble-counting, volume-by-number, grid-by-number, and area-by-number methods [11,12]. However, those methods are time-consuming and expensive, providing inadequate, point-like local data. In cases where the composition of the riverbed is highly mixed and the gravel-dominated bed is transformed into a sand bed, those methods are not representative enough. River beds characterized by inhomogeneous composition in conjunction with the growing interest for an increase in the sampled area accompanied

by reduced field effort require map-like information, which nowadays can be provided through the combination of digital imagery with image analysis [13].

In particular, river research studies have increasingly initiated utilizing UAV imagery, which can offer centimeter precision and capture a vast quantity of data points in a short time, covering large areas [14]. Correspondingly, image processing techniques, developed in the last decades, were established as highly acceptable methods for automated grain size data extraction from digital images of river beds [15–20]. Sediment grain size can be evaluated using remote sensing technologies and image analysis techniques, including pixel and OBIA [21]. Nowadays, pixel-based classification is limited as it produces inconsistent classification results dealing with the rich information of high-resolution data, e.g., UAV imagery [21]. However, OBIA utilizes object features, such as texture, forms, and spectral information for segmentation and classification, while it was proven that OBIA classification algorithms are more accurate, precise, and provide a greater estimation probability of the statistical properties of an image in comparison with pixel-based image processing [14]. One of the first developed local image properties, capable of segmenting image areas, is the texture evaluated with the co-occurrence matrix [22–24]. A raw image is transformed through texture-based analysis to a textural image while the regional texture information corresponds to gray levels [25]. Co-occurrence has the ability to quantify how many pixels of similar gray levels are neighbors; hence, provided that image resolution is sufficient, it is considered that image texture facilitates the grain size determination since distinct different grain sizes are apparent [25].

Input data uncertainty is one of the most important sources of epistemic uncertainties involved in flood inundation modeling [26]. Two major sources of input data uncertainty in hydraulic–hydrodynamic modeling applications are the DEM accuracy and the roughness coefficient value determination [27]. A common methodology followed for indirect estimation of Manning’s n roughness coefficient values at ungauged catchments is the evaluation of the river bed materials type and size based on field observations and photographs of the study area [28]. However, the uncertainty associated with the above-mentioned indirect method of Manning’s n roughness coefficient value estimation has led to the usage of other techniques such as the Wolman pebble count method [29], grid sampling method [8], and aerial sampling method [8] that estimates the grain size. It is important to highlight that a typical approach followed in such cases is using empirical formulas where the particle size estimation is a key-point parameter. Using particle size estimation methods in combination with empirical formulas minimizes the objectivity involved in Manning’s n estimation. The limitation of the methods mentioned above is that the estimated roughness value is restricted only at the sampling area (e.g., estimation of separate roughness values for each sample grid). Therefore, even though Manning’s n can be estimated in a better way using such methods mentioned above, the estimation of spatially distributed Manning’s n values for an entire stream reach still remains a challenging issue. As mentioned earlier, many of the limitations can be overcome using Unarmed Aerial Systems (UAS) that allows the production of high-resolution images and DEMs.

Another epistemic uncertainty involved in flood modeling and mapping is the applied hydraulic modeling structure (1-D, 2-D, 1-D/2-D) [30]. The simplicity, low computational power, and limited demands of input data rank the one-dimensional hydraulic models as the most utilized modeling approach in river flood modeling applications (e.g., [31–34]). Moreover, the usage of two-dimensional hydrodynamic models has risen dramatically due to improvements in model parameter estimation methods, model structure, and other related technological advancements [32,35–37]. Finally, river flood modeling applications using coupled 1-D/2-D models have gained significant acceptance in the scientific community due to the combination of the capabilities of 1D and 2D models [32,38,39].

According to the paragraphs mentioned above, it can be concluded that the objective determination of roughness coefficient in river flood modeling remains a crucial issue. Moreover, sensitivity analysis in flood inundation modeling using different hydraulic modeling approaches and/or combined with spatially distributed roughness coefficient

maps is a subject that still concerns the scientific community [40–43]. The main purpose of this paper is to present an objective way to determine Manning’s n roughness values, remotely-sensed estimated, and indicate how the changes in those values may affect a flood extent. Both pixel-based and OBIA techniques were investigated to sufficiently classify the dominant substrate grain sizes by using RGB (Red, Green, and Blue) images, obtained via UAVs, and ground truth grain size data. Grain size classification accompanied by predefined diameters, land use data, and empirical formulas contributed to the generation of spatial distributed Manning’s n roughness coefficient maps. Another objective of this work is to examine the sensitivity of different hydraulic–hydrodynamic modeling approaches (1D, 2D, 1D/2D) and Manning’s n roughness coefficient scenarios on floodplain mapping and flood inundation modeling at ungauged gravel-cobble bed streams. The simulated flooded area validation was accomplished using historical flood extent data, the CSI, and penalized CSI. The methodological framework was implemented at the ungauged Xerias stream reach, Volos, Greece.

2. Materials and Methods

Towards the investigation of Manning’s n roughness coefficient estimation followed by the sensitivity analysis of floods using different hydraulic/hydrodynamic modeling approaches (1D, 2D, 1D/2D), several methodological approaches followed (Figure 1): (1) fieldwork including the UAV flight and grid sampling along 11 sampling grids that were equally distributed in the entire stream reach of 2.2 km in representative locations; (2) dominant grain size classification along Xerias stream based on local entropy values, estimated from UAV’s obtained RGB images; (3) generation of the spatial distributed Manning’s n roughness coefficient maps based on size–frequency distributions of bed-materials, land use data and empirical formulas; (4) estimation of the flood extent by adopting 1D, 2D and coupled (1D/2D) hydraulic modeling approaches and its validation by using historical flood extent data, the CSI, and penalized CSI.

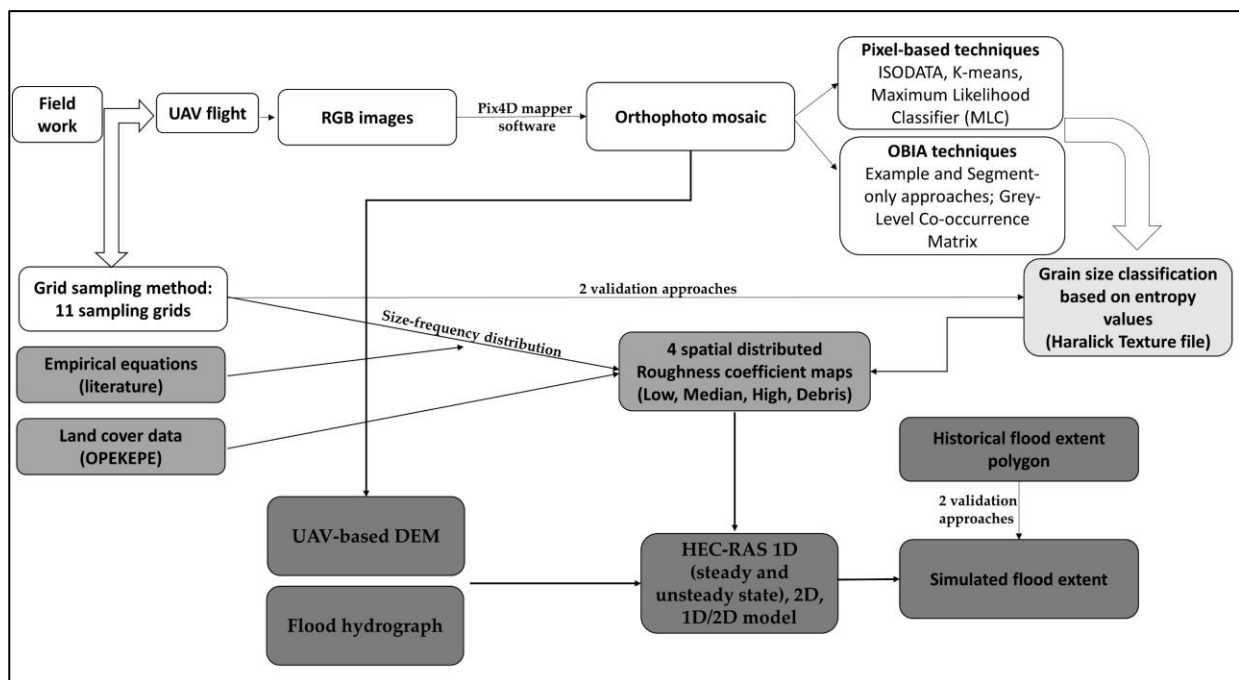


Figure 1. Flowchart of research methodology steps. Different shades of grey color represent the distinct methodological approaches (the three grey shades ranging from light to dark grey represent the grain size classification based on entropy values, the generation of the spatially distributed roughness coefficient maps, and the estimation of the flood extent, respectively).

2.1. Study Area

The study stream reach (Xerias stream), with a length of 2.2 km, is located at the suburban region of Volos city, south-eastern part of Thessaly region, Magnesia prefecture, Greece (Figure 2a). The stream reach lies between latitude 39.397251 to 39.380332 N and longitude 22.916315 to 22.929220 E. The stream reach altitude ranges from 22 to 52 m, while the gradient of the stream reach is approximately 0.014 m/m. There are three (3) bridges in a row with variable length and width at the specific stream segment. The watershed area up from the specific stream segment of Xerias is approximately 71 km². The altitude of the specific watershed ranges from 52 to 1600 m, and the mean slope of the area is 28%. The largest part of the specific watershed is covered mainly by forest and semi-natural areas (80.47%) and agricultural areas (19.54%). The selection of the stream reach is based on the existence of typical bed material usually observed in mountainous and semi-mountainous streams and the complexity of the river topography (Figure 2b,c). In particular, Xerias is a gravel- and cobble-bed stream, which is a typical characteristic of intermittent flow streams experiencing flash flood events. The torrential character of the specific stream reach and the river bed is unchanged in the last decades and without severe manmade interventions. Moreover, the Xerias stream, draining through the city of Volos, has experienced frequent flood episodes due to intense storms. In October of 2006, the city of Volos in Magnesia, Greece, was impacted by an extreme flash flood event that damaged several technical infrastructures, transportation networks, and agricultural areas throughout the Xerias River watershed. During this flash flood event, the heavy rainfall, equal to 232 mm, that lasted approximately 12 h caused extended fluvial flooding [41]. It is important to note that the railway bridge, which is located within the study area, collapsed during this flood event. Details of the observed historical flood event of 9 October 2006 and the watershed characteristics can be found in recent studies [30,41,44,45].

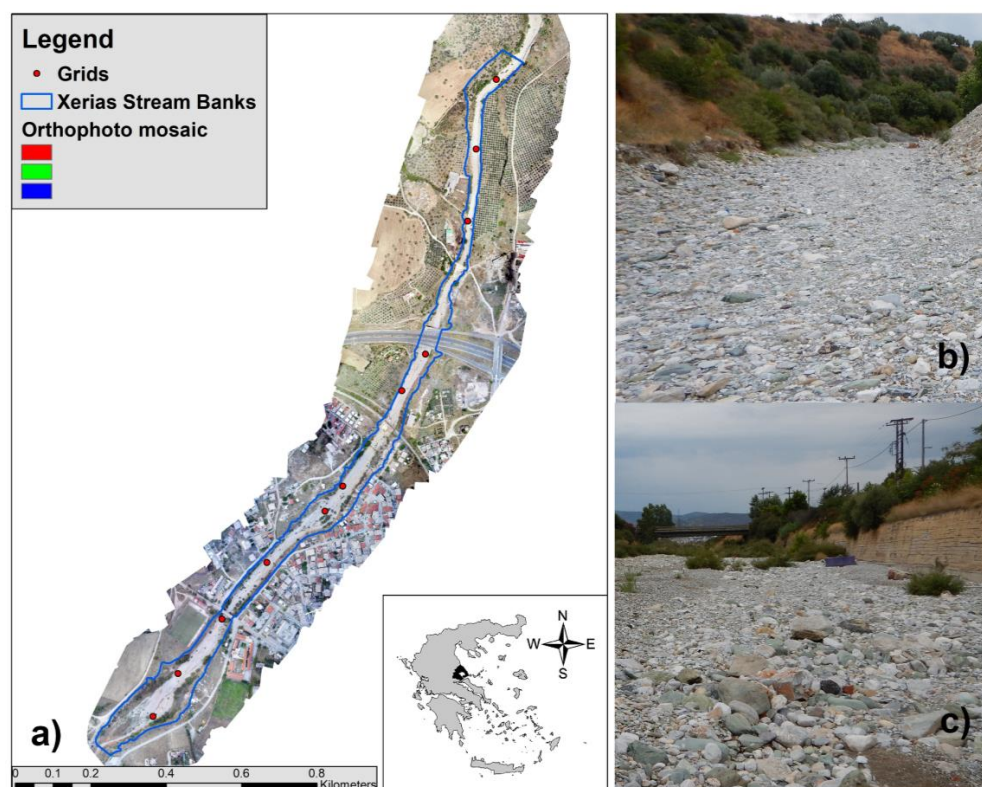


Figure 2. Xerias stream reach (red dots represent the location of the sampling grids) (a) and inhomogeneous bed composition (b,c).

2.2. Data, Ground Truth, and Tools Applied

The topographic field data in the study area were collected on 18 July 2019 by using a DJI Phantom 4 V2 Professional UAV. The first stage of the photogrammetric study involved the installation of Ground Control Points (GCPs) on the land and the flight operations, while the second one comprised the office work. Thirty-nine GCPs were homogeneously distributed around the study area and were measured before the UAV flight using the topographical SP60 (Spectra corporation) Global Navigation Satellite System (GNSS) receiver. During the office work, overlapping pictures were introduced in the Pix4D mapper software to apply photogrammetric algorithms and develop the area's Digital Surface Model (DSM) and the Digital Terrain Model (DTM). The camera's resolution was 20 MP, while the percentage overlap for adjacent pictures was 80%. The area covered during the field survey was approximately 2200 m × 300 m (length × width) along the river course, and the flight altitude was 40 m. The Pix4D photogrammetric process steps include the estimation of the UAV's camera parameters for image calibration and bundle adjustment, the extraction of identical image points (tie points) among the overlapping pictures, the estimation of the 3D point cloud, and the built-up of the DSM. The photogrammetry algorithms are analytically described in Unger et al. [46], and the mean error of the reconstructed surface is approximately 1–3 times the ground sampling distance [47]. The cell size of the produced DTM was approximately 0.013 m, which corresponds to a potential inherent error between 0.013 m and 0.04 m. Finally, some small modifications were implemented in the produced DTM to better represent the hydraulic works in the study area (three bridges in a row and some retaining walls) and to eliminate any remaining distortions caused by vegetation or buildings that were involved in the flood inundation area domain. The overall accuracy of all photogrammetric products was evaluated using the GCPs, which were identified in the orthoimages, and their coordinates were compared to the surveyed GNSS coordinates resulting in a total Root Mean Square (RMS) error of 0.042.

Among the numerous surface sampling methods, the typical grid sampling method [8] was used because it can provide accurate results [8]. Bed-material sampling in cobble- and gravel-bed streams, as Xerias stream, is a more complicated task than sampling in sand- and boulder-bed streams forcing the researcher to pre-decide the sampling method depending on the study's objective and the stream condition [6]. The grid sampling method can be used to estimate predefined particle diameters, which is an essential component in Manning's roughness values estimation. Different techniques can be used to sample the surface particles. In this study, particles were collected along grids, sampling frames covering a surface of 1 m² [8]. In order to examine the bed material in a sufficient way, 11 sampling grids were equally distributed in the entire stream reach of 2.2 km (Figure 2) in locations representative for the under-study stream. In order to minimize the sampling time, the more oversized bed materials with minimum size 10 to 15 cm were measured within the stream and were picked off the stream surface (pebble count; Figure 3a–c) while the bed material of smaller size was collected and measured at the laboratory facilities (Figure 3d). The three mutually perpendicular particle axes that were measured are: the longest (a-axis), the intermediate (b-axis), and the shortest (c-axis) axis. All length measurements were accomplished using a digital caliper (Figure 3d). Finally, the grid count data were classified based on the Wentworth scale (Table 1; [8]) depending on the actual b-axis length (in units of cm), the longest intermediate axis perpendicular to the a-axis as performed in the Canadian guidelines [48].

Table 1. Grid count data classification based on Wentworth scale [8].

Substrate Type	Size (cm)
Sand-mud	0.0062–0.2
Gravel	0.2–6.4
Cobble	6.4–25.6
Boulder	25.6–409.6
Bedrock	>409.6



Figure 3. Grid sampling method of 1 m² [8] applied in grids of inhomogeneous bed composition (a–c) and axes measurements at laboratory facilities (d).

2.3. Dominant Grain Size Classification via Airborne Image in Streams: Tested Methods

Prior to the primary analysis, the orthophoto mosaic (Figure 2a) was converted from RGB to HSV (hue, saturation, value), HLS (hue, lightness, saturation), and intensity bands by using the ENVI v.5.5 software in order each band of R, G, and B as well as H, L, and S be investigated concerning their contribution to image segmentation. Subsequently, various image processing methods were explored for substrate classification, specifically applied to the lower part of the Xerias stream (2.2 km; Table 2). The majority of the increasingly used methods in river morphology measurements are based on either pixel-based image analysis or OBIA. Initial experiments on pixel-based image analysis included several supervised and unsupervised classification methods. The MLC, the ISODATA, and K-Means algorithms of the ENVI v.5.5 software were investigated to recognize the dominant existing sediment classes of the orthophoto mosaic, spatially clipped at the main riverbed's boundaries.

Table 2. Tested methods and approaches for dominant grain size classification applied to the lower part of Xerias stream.

Approach	Method	Tool	Anticipated Result
Pixel-based image analysis	Supervised/Unsupervised classification	ISODATA, K-means, Maximum Likelihood Classifier (MLC)	Pixel-based classification map
Object-based image analysis (OBIA)	ENVI feature extraction module (ENVI v.5.5)	Example and Segment-only approaches	Object-based classification map
	Local image texture analysis (QGIS v.3.18)	Grey-Level Co-occurrence Matrix (GLCM)	Reclassified entropy values (Band 2) interpreting grain size classes

As far as the OBIA is concerned, trials initially adopted the ENVI feature extraction module, which extracts information from high-resolution imagery based on spatial, spectral, and texture characteristics using an object-based approach. Among the available approaches that the ENVI feature extraction module offers, the example-based (based on supervised and unsupervised classifications) and the segment-only ones were investigated. Significant parameters that were repeatedly modified and tested are the type of segment (segment bands) and merge algorithms (merge bands), the scale and merge levels, the type of Lambda schedule, and the texture kernel size in pixels. A crucial role in image segmentation analysis plays the pre-definition of the mentioned above parameters' because user judgment is involved in the process. Thus, the definition of certain characteristics such as features boundaries (distinct or not), features merging (small features with larger or with other features with similar colors and border sizes, etc.), and further delineation (properly delineated features) are based on the user judgment and experience. Equally significant is the final selection of the classification method; either the K Nearest Neighbor (KNN) or the Support Vector Machine (SVM). Especially in the SVM classifier, the kernel type should be defined, and the available selections are the polynomial, sigmoid, and the radial basis function.

Final attempts were made to segment and classify the Xerias stream-bed substrate based on Local image texture analysis. Second-order textures are based on the grey-level co-occurrence matrix (GLCM) [49], and according to this method, the texture is developed on a set of statistics derived from a greater group of local image properties. The respective literature [14] has indicated the GLCM method as the main technique to analyze the texture; therefore, in this study, a second-class texture measure of a GLCM was conducted. The Simple Haralick Texture file was extracted by using the QGIS V.3.18 software, including the following eight texture measures represented by bands: energy, entropy, correlation, inverse difference moment, inertia, cluster shade, cluster prominence, and Haralick correlation. Moreover, Ricard and Bercovici [50] affirmed that the continuous and discontinuous processes of grain size distribution are determined by nonequilibrium thermodynamics. In particular, entropy production can interpret the phenomenological laws for grain growth and reduction. Based on this rationale and taking into consideration that in similar efforts [14,25], the texture measure of entropy was utilized to map surface grain size in bed rivers, in this study, the band of entropy was reclassified to interpret the grain size classes along the Xerias stream. Furthermore, it should be noted that all the above-mentioned trials in several parameters and their multiple combinations were applied either on RGB image, or HLS/HSV images, or separate red and intensity bands.

The qualitative capability of the developed method to classify and map the stream bed's sediment was evaluated in two ways. First, according to field measurements, 240 random points were created and equally distributed through the common QGIS tool among the three known grain classes (boulder, cobble, gravel). Concerning the assessment of classification accuracy derived from remote sensing techniques, creating random points is widely used [51]. Followingly, checks were carried out to estimate the percentage agreement between the coincident field measurements and the respective remotely sensed sediment classes. The second way of validation involves the grain shape assessment of the field measurements and the usage of typical sediment area shape formulas to estimate each grain class's area percentage for each grid. The comparison between the estimated area percentage based on the field measurements and the generated surface grain size classified map provided the percentage of correct classification.

2.4. Manning's n Roughness Coefficient Estimation Methodology

A typical approach followed for determining Manning's roughness values is the combination of field observations, personal judgment, photographic roughness estimates, and typical values retrieved from the literature [28]. However, this approach involves major uncertainties that enter in flood inundation modeling due to the objectivity of the user and the fact that photographic roughness estimates are intended for a given depth of flow (can be inappropriate for all settings) [29]. Therefore, to minimize the limitations mentioned above, the grid sampling as shown in Figures 2a and 3 is used for the estimation of the final Manning's n values. As already mentioned, the grid sampling method is a common approach followed for assessing particle size in gravel-bed and cobble-bed torrents [8].

Table 3 presents the empirical equations proposed in the international literature for estimating Manning's roughness coefficient. Details on the parameterization of the selected empirical relationships and their usage can be found in previous works of the authors [27,30]. According to the selected empirical equations, the predefined diameters of D_{50} , D_{65} , D_{84} , and D_{94} were estimated based on the grid sampling methodology [8]. All empirical relationships (Table 3) were used to determine the river bed Manning's roughness values. Therefore, boulder, cobble, and gravel Manning's roughness values were estimated based on the combination of the grid sampling results with all empirical relationships. Thus, the riverbed roughness coefficient was defined for each category using the minimum, median, maximum values, and the maximum value increased by 20% derived from the process mentioned above.

The estimation of Manning's n roughness value for the areas adjacent to the river bed and the floodplain were based on the common approach of using land cover data and

roughness coefficient tables (e.g., [52–54]). The Greek Payment Authority of Common Agricultural Policy Aid Schemes (OPEKEPE, in Greek) land cover data (1:5000 scale) [55] were used to classify the adjacent river and floodplain areas. Finally, the spatially distributed roughness coefficient was derived by using the estimated roughness coefficient values in combination with the classified river bed and the land cover data. In this study, four different roughness coefficient scenarios were set up based on the minimum, median, maximum, and maximum value increased by 20% (from now on referred to as debris scenario). For comparison reasons, a fifth scenario demonstrated using a single roughness value for the entire riverbed and a single roughness value for the entire floodplain. Therefore, the Manning’s n roughness values of the fifth scenario were defined based on the median roughness values of the optimum scenario that derived from the analysis of the four basic scenarios mentioned above. The examined scenarios aimed to quantify the uncertainty induced by the estimation of the roughness coefficient.

Table 3. Empirical relationships proposed by the international literature for assessing Manning’s roughness coefficient (n) values.

A/A	Equation	Reference
1	$n = 0.0431D_{90}^{1/6}$	[56]
2	$n = 0.0439D_{90}^{1/6}$	[56]
3	$n = 0.0593D_{50}^{0.179}$	[57]
4	$n = 0.0561D_{65}^{0.179}$	[57]
5	$n = 0.0495D_{90}^{0.16}$	[57]
6	$n = \frac{D_{90}^{1/6}}{15.29}$	[58]
7	$n = \frac{D_{90}^{1/6}}{16}$	[58]
8	Gravel, $n = 0.028–0.035$ Cobble, $n = 0.03–0.05$ Boulder, $n = 0.04–0.07$	[59]
9	$n = \frac{0.1129R^{1/6}}{1.16 + 2 \log(R/D_{84})}$	[29]
10	$n = \left[0.183 + \ln \left(\frac{1.762S_f^{0.1581}}{Fr^{0.2631}} \right) \right] \left(\frac{D_{84}^{0.167}}{\sqrt{g}} \right)$	[60]
11	$n = \left[0.183 + \ln \left(\frac{1.7462S_f^{0.1581}}{Fr^{0.2631}} \right) \right] \frac{(D_{84})^{1/6}}{\sqrt{g}}$	[61]
12	$n = \left[0.183 + \ln \left(\frac{1.3014S_f^{0.0785} \left(\frac{R}{D_{84}} \right)^{0.0211}}{Fr^{0.1705}} \right) \right] \frac{(D_{84})^{1/6}}{\sqrt{g}}$	[61]
13	$n = \left[0.219 + \ln \left(\frac{1.3259S_f^{0.0932} \left(\frac{R}{D_{50}} \right)^{0.026}}{Fr^{0.2054}} \right) \right] \frac{(D_{50})^{1/6}}{\sqrt{g}}$	[61]

n = Manning’s n roughness coefficient (m³/s), R = hydraulic radius (m), D_i = characteristic size of bed material, which is larger than i% of particles (m), S_f = energy slope (m/m), Fr = Froude number, g = acceleration due to gravity (m/s²).

2.5. Hydrodynamic Modeling Configuration

HEC-RAS (Hydrologic Engineering Centers River Analysis System) is a worldwide acknowledged hydraulic–hydrodynamic model with much scientific literature and practical applications. A plethora of studies used HEC-RAS 1D for flood inundation modeling

applications [27,40,62–65]. Recent updates of HEC-RAS allow two-dimensional (2D) and coupled (1D/2D) modeling with many successful applications [36,45,66–72]. The capabilities and the efficiency of the two-dimensional (2D) HEC-RAS model were tested by Brunner and CEIWR-HHT [53,73]. Therefore, the sensitivity analysis of floods using different hydraulic/hydrodynamic modeling approaches (1D, 2D, 1D/2D) was implemented using the HEC-RAS v.6.1 hydraulic–hydrodynamic model.

The upstream boundary conditions in all modeling approaches are based on Papaioanou et al.'s previous work [30,44] and concern the extreme flash flood event in 2006. Thus, the flood hydrograph used in this study (Figure 4) is based on the Clark Instantaneous Unit Hydrograph (CIUH) methodology, which is a typical methodology followed for streams without flow records (ungauged catchments) [30,41,44,45]. The maximum value of the flood hydrograph is $490.43 \text{ m}^3/\text{sec}$. Several other configurations and model parameters, such as the downstream boundary conditions, were determined in agreement with HEC-RAS standards [53,74].

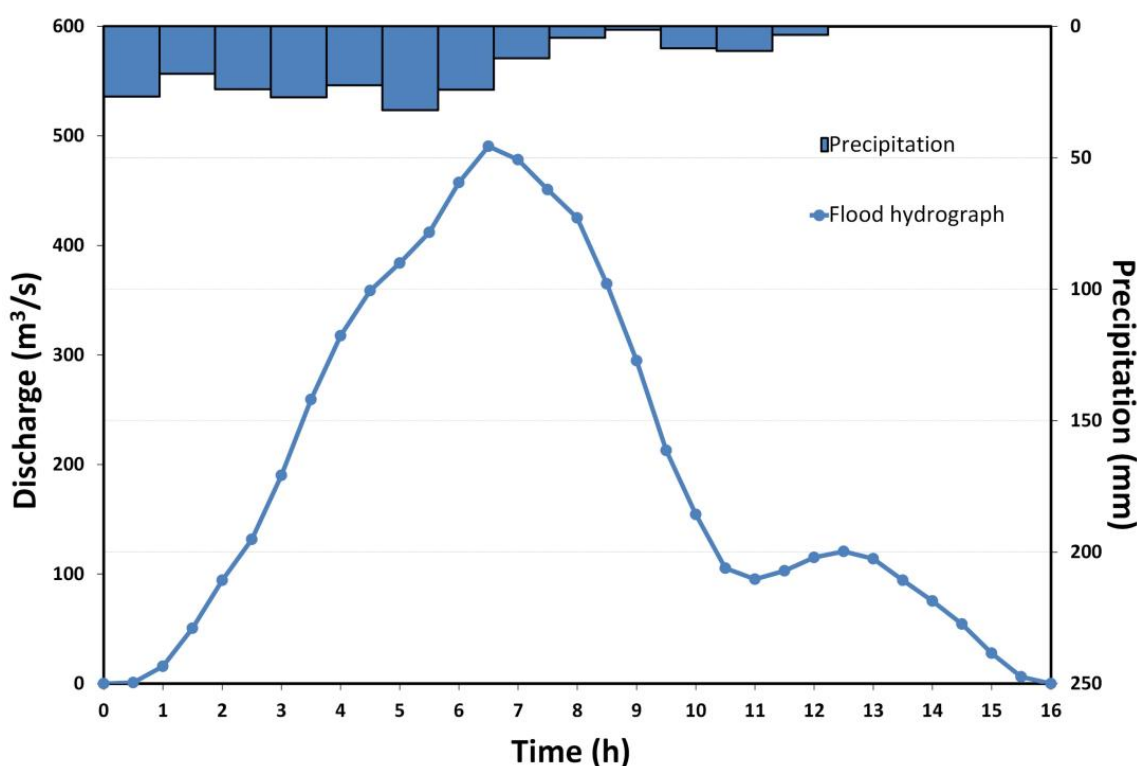


Figure 4. The rainfall hyetograph of the 9 October 2006 and the estimated flood hydrograph of the event by applying the Clark Instantaneous Unit Hydrograph (CIUH) method (Adapted from [27]).

River and adjacent areas' geometry representation is crucial in flood inundation modeling and mapping, especially in areas with complex terrain and limited floodplain [75–78]. In this study, a high-resolution UAV-derived DEM was used to represent the river and riverine area accurately for river flood modeling (Figure 5). The roughness coefficient configuration is based on the methodology presented in Section 2.4. It is noteworthy to mention that due to software limitations in 1D modeling, the maximum available roughness value per cross-section is twenty. In addition, the resolution of the generated spatial distributed roughness coefficient maps was set to 0.5m for simulation stability issues. Therefore, five different flood modeling scenarios are configured for each modeling approach based on the spatially distributed roughness coefficient maps. In the one-dimensional modeling approach, both steady and unsteady flow simulations are implemented.

Some other significant characteristics of the HEC-RAS 2D model configuration are: (1) two-dimensional flow area computational point spacing set from 5 to 10 m with average cell 8m (Around the bridges and the retaining walls a denser mesh was generated); (2) the

default modeling solutions were used for all flood inundation modeling applications; (3) advanced time step control using adjust time step based on Courant was used with initial time step one (1) second; (4) several breaklines were used for better representation of the hydraulic structures, the banks, and the main stream; (5) all bridges (Figure 5) were configured as structure type bridges, even in two-dimensional modeling approach; (6) the cross-sectional spacing was set to 60m (Figure 5) due to stability issues and in accordance to the HEC-RAS standards [53,74]; (7) In coupled (1D/2D) modeling approach the normal 2D equation domain was selected in overflow computation method due to stability issues and in accordance to the HEC-RAS standards [53,74].

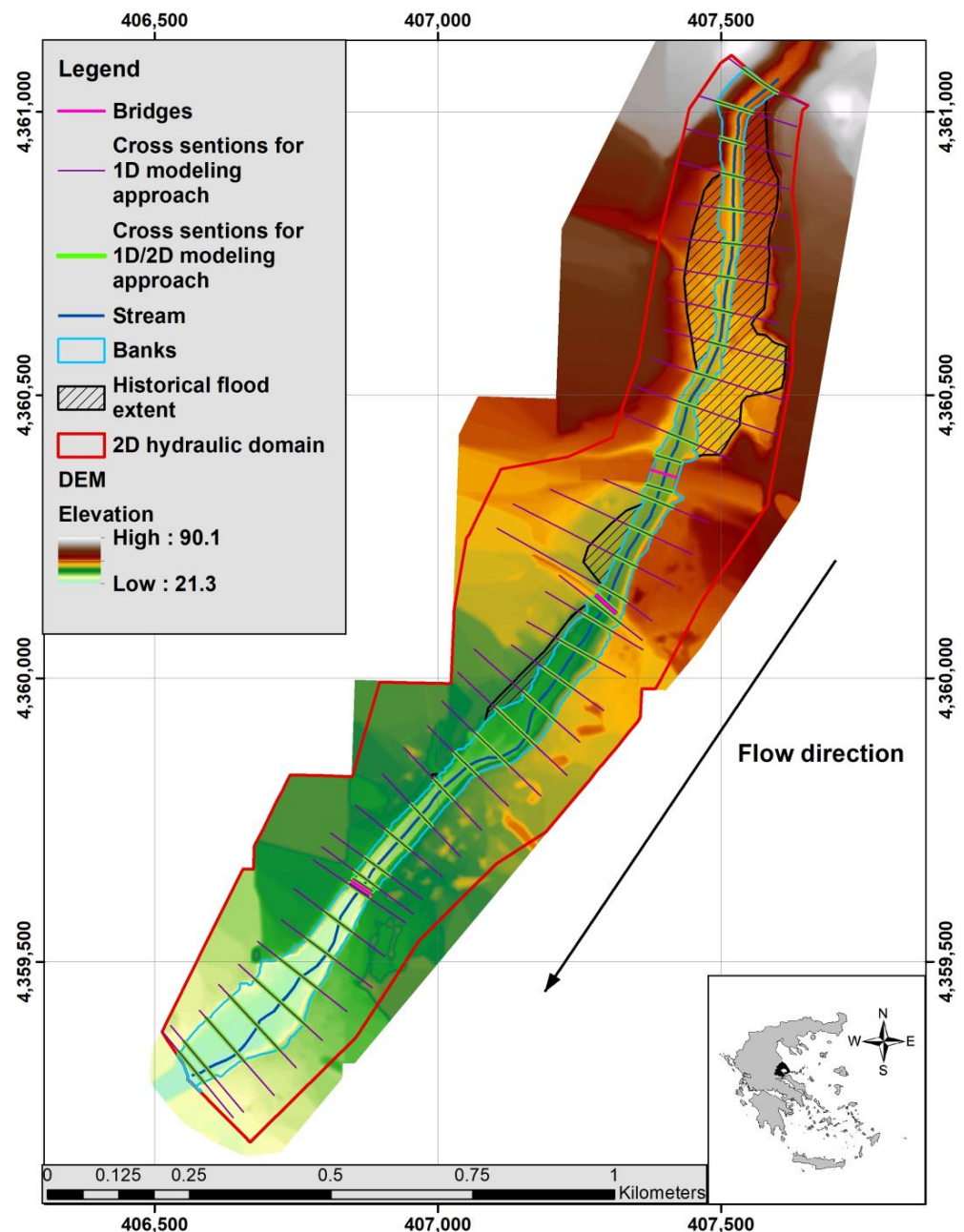


Figure 5. Xerias stream hydraulic modeling domain.

Typical indices based on flood extent were used for the evaluation of flood inundation modeling performance [79–81]. A validation polygon (Figure 5) that is based on historical records and data was used in the modeling performance process. Specifically, since the authors did not find any Judicial reports or other flood-related data sources for the study

flood event, the validation polygon was derived from several interviews with local people who experienced the flood event (no interviewee was able to provide accurate water depth values) (details for the flood extent data can be found in [27,30,41,45]). Thus, the Critical Success Index (CSI) or threat score (TS) [80–83] and the penalized CSI [68,79–81] were chosen for the assessment of the simulated inundated areas against the validation polygon. From now on as F1 and F2 will be denoted the CSI and penalizing CSI, respectively. The estimation of both F1 and F2 is based on the 2×2 contingency table for all grids areas as follows:

$$F1 = \frac{A}{A + B + C} \quad (1)$$

$$F2 = \frac{A - B}{A + B + C} \quad (2)$$

A is the correctly predicted flooded area (hits), B is the flooded area false prediction (false alarms), C is the flooded area that is not predicted by the model (misses). The term B at the numerator in Equation (2) is used to penalize the model's overprediction [79].

3. Results

3.1. Sediment Grain Size Analysis and Classification

3.1.1. Sediment Grain-Size Distributions (Field Measurements)

Figure 6 presents the cumulative grain-size distributions obtained by grid sampling of 11 grids. According to the grid sampling analysis, the river bed materials are categorized as very coarse gravel with a median value of 32.4 mm. Therefore, the river bed materials are basically dominated by gravels followed by cobbles (Figure 6). Table 4 presents the estimated predefined diameters for each river bed class which are essential parameters in the roughness coefficient estimation.

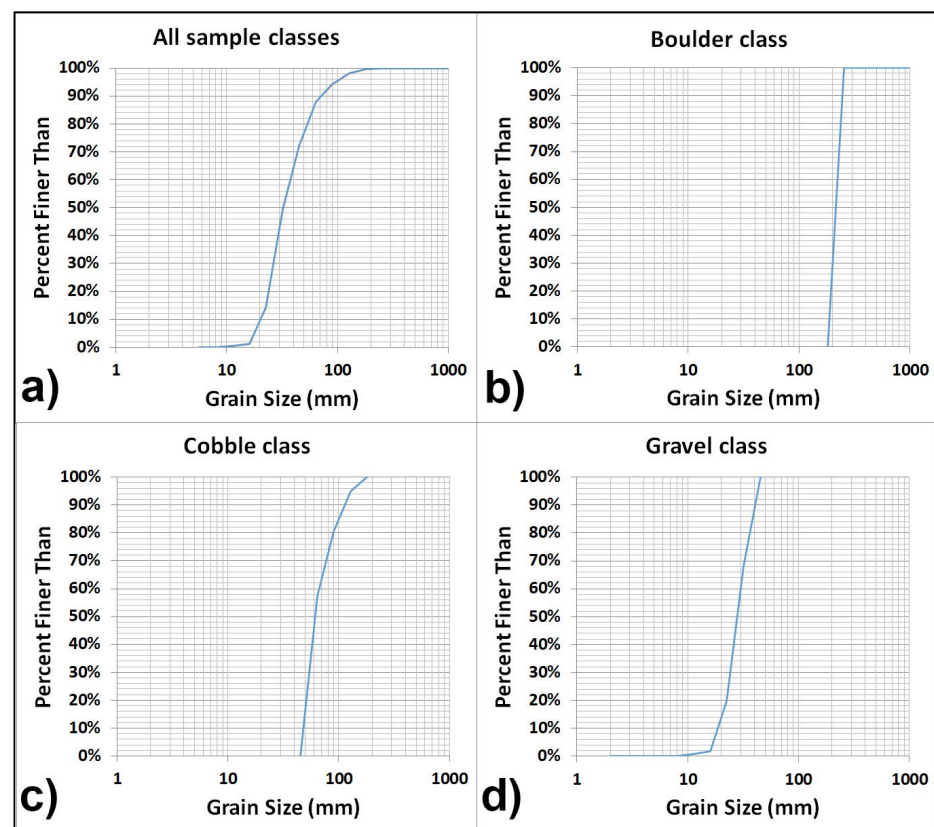


Figure 6. Cumulative grain-size distributions obtained by grid sampling of 11 grids concerning: all samples count (a), only boulder count (b), only cobble count (c), only gravel count (d).

Table 4. Estimated predefined diameters for each river bed class.

	Predefined Diameters	ds, (m)		Predefined Diameters	ds, (m)		Predefined Diameters	ds, (m)
Gravel	D ₅₀	0.028	Cobble	D ₅₀	0.062	Boulder	D ₅₀	0.219
	D ₆₅	0.031		D ₆₅	0.073		D ₆₅	0.230
	D ₈₄	0.039		D ₈₄	0.100		D ₈₄	0.244
	D ₉₀	0.041		D ₉₀	0.115		D ₉₀	0.249

3.1.2. Sediment Grain Size Classification via Image Analysis

The majority of the numerous classification trials resulted in ambiguous results, while the following experiments (Table 5) presented are those characterized by the greater classification accuracy based on sampled, ground truth grain size data. Tested unsupervised classification algorithms (i.e., ISODATA, K-MEANS) tried to automatically group pixels of similar spectral features into unique clusters without reliable classification as identified by visual inspections. On the other hand, spectral signatures of well-known classes were created based on high-resolution photos taken at the field and were utilized as training data for the MLC. Based on them, MLC managed to distinguish with great reliability both riparian vegetation and the vegetation detected in the middle of the stream-bed. A little less accuracy was ascertained concerning the detection of boulders and bedrock classes. More specifically, MLC succeeded in detecting the location of those classes but not providing their full areal extent.

Table 5. Pixel- and object-based image analysis methods that indicated better classification results.

Approach/Method	Bands	Results and Set Parameters
Pixel-based image analysis/ Maximum Likelihood Classifier	RGB	<u>Riparian vegetation and the vegetation detected in the middle of the stream-bed</u> <u>Boulders and Bedrock</u> classes
Object-based analysis (OBIA)/ ENVI feature extraction module	RGB	<u>Boulders</u> (full lambda; 35 scale value; 50 merge value; SVM) <u>Cobbles</u> (polynomial kernel type/ radial basis function)
	Red and Intensity	<u>Gravels</u> (SVM; radial or polynomial kernel type)
Object-based analysis (OBIA)/GLCM	Haralick Texture file (Entropy band)	<u>Cobbles, Gravels, and Sand-mud</u>

Stream-bed classifications originating from the ENVI feature extraction module also presented results characterized by low accuracy. The application of mainly edge segment algorithm accompanied by the various scale and merge values ranging from 20 to 40 and from 30 to 80, respectively, applied separately on RGB (Figure 7a), HSV, red, and intensity bands were explored. In particular, among them, better classification results were retrieved with full lambda merge algorithm, scale value 35 and merge value 50. Those set parameters yielded even better results concerning the class of boulders when they were accompanied by the SVM classification method and polynomial kernel type or radial basis function regarding the class of cobbles. Gravels were better classified when only the red and the intensity bands were inserted and accompanied by the SVM classification method and radial or polynomial kernel type, respectively. HIS and RGB images' segmentation associated with SVM and radial or polynomial kernel type gave poor classification results. Even though the aforementioned classifications were superior to the rest ones, they still do not constitute a reliable means for grain size classification.

Final experiments included the reclassification of the entropy band retrieved from the Haralick Texture file, which proved to be the most optimal way to interpret the grain size classes along the lower part of Xerias stream (Figure 7b). Microstructure entropy values managed to constitute a function of the grain sizes, particularly of cobble, gravel, and sand-mud classes (Figure 7c). Unfortunately, the boulder class was not interpreted with

adequate accuracy by entropy values; thus, this class was established based on MLC results and further digitization in ArcMap. Final classification results based on entropy values indicated the cobbles and gravels as the most dominant classes along the study area (by percentages of 45.7% and 50.5%, respectively). The class of sand-mud constituted 1.6% of the total studied area while the boulder and bedrock classes (based on MLC and further digitization) represented 0.84% and 1.4%, respectively, of the lower part of Xerias stream.

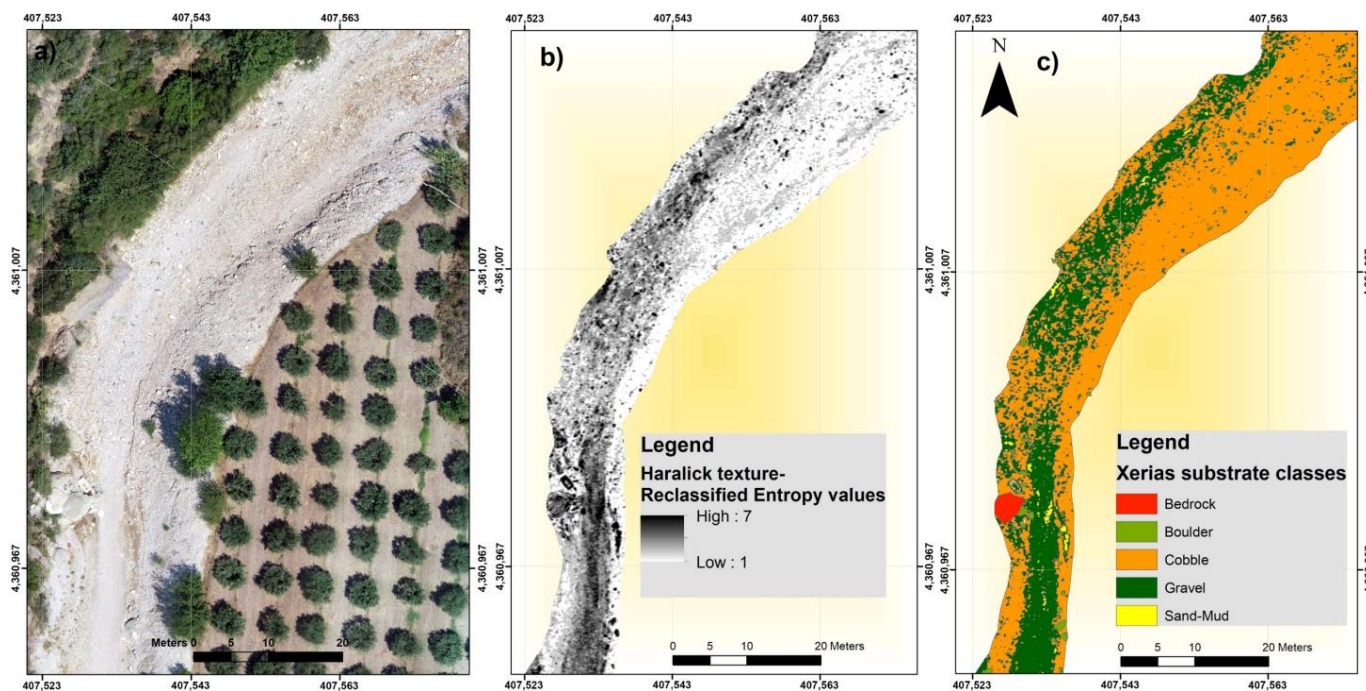


Figure 7. Orthophoto mosaic: (a) Simple Haralick Texture (entropy band) (b) and Stream-bed substrate classification (c) of a northern part along Xerias stream.

The accuracy of the applied hybrid classification method was assessed using a total of 240 random points, which were equally distributed across the 11 sampling grids while the class values were attributed according to ground truth data concerning the three known grain classes (boulder, cobble, gravel). The total accuracy achieved is 65%, accompanied by 156 points correctly classified. In particular, it was observed a 0 out of 16 coincident points in boulders, 143 out of 152 coincident points in cobbles, and 13 out of 72 coincident points in gravels, according to field measurements. The second evaluation method involved a shape analysis implemented to define the dominated particle shape in the entire study area (Figure 8). The results from the grain shape assessment analysis (Figure 8) showed that based on the categorization method of Zingg [84], the study site consists of disk-shaped sediments. The average b/a and c/b values of the dataset were 0.69 and 0.53, respectively (Figure 8, black +). Then, the typical sediment area shape formulas were used to estimate the area percentage of each grain class for each grid (field), and their comparison with the generated surface grain size based on the classified map provided an average overall 52% correct classification.

3.2. Manning's Roughness Coefficient Estimation

In this study, the river bed roughness coefficient was estimated using the stream-bed substrate classification and several empirical formulas. The roughness coefficient of the adjacent river areas and the floodplain was determined using detailed land cover data (OPEKEPE) and values estimated from the literature. The spatially distributed land cover and stream bed map is presented in Figure 9. Table 6 presents the estimated Manning's roughness coefficient values from both classification procedures and the four basic roughness scenarios that were used in river flood modeling. Finally, the combination of data

presented in Figure 9 and Table 6 generated the four basic different spatial distribution maps that were used in the flood inundation modeling application. Specifically, according to Table 6 and field CODE, 1 to 5 categories concern the estimation of roughness coefficient based on the combination of empirical equations and the remote sensing methodology, while in the rest categories (from 6 to 17), the roughness coefficient was estimated based on the OPEKEPE land uses and values estimated from the literature. It is noteworthy to mention that the Bedrock class received the value of 0.013 because the observed bedrock parts are constituted of concrete. The roughness coefficient values of the fifth scenario were defined as the median values of the riverbed components and floodplain components, respectively, of the high roughness scenario that seems to have a better response according to the evaluation criteria presented in the following paragraphs. Therefore, for the fifth scenario, the riverbed roughness was set to 0.068, and the floodplain roughness was set to 0.055.

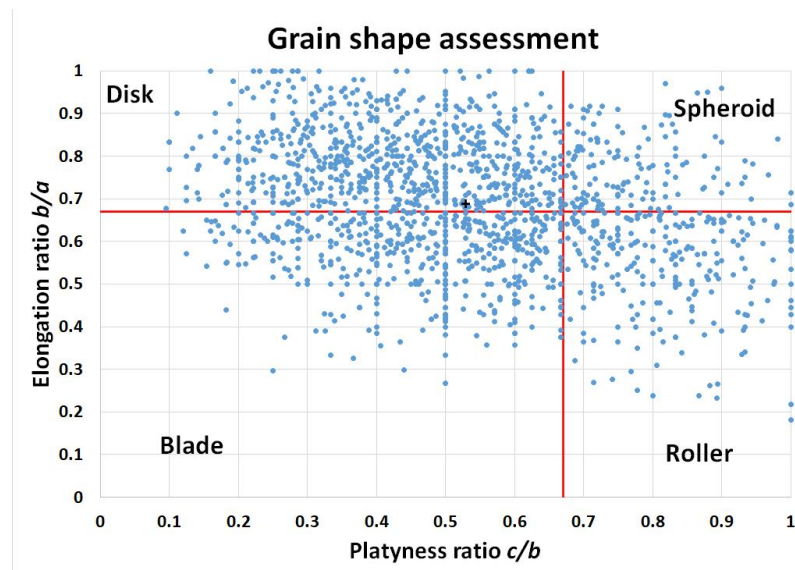


Figure 8. Grain shape assessment results (with blue dots) and the calculated average shape (marked with black +).

Table 6. Manning’s n roughness values for all scenarios and all classification categories.

CODE	Classification Category	Manning’s n Scenarios			Debris
		Low	Median	High	
1	* Bedrock	0.013	0.013	0.013	0.013
2	Boulder	0.0301	0.0414	0.082	0.0984
3	Cobble	0.0265	0.035	0.073	0.0876
4	Gravel	0.0223	0.0297	0.068	0.0816
5	Sand-Mud	0.026	0.0305	0.035	0.042
6	Medium size vegetation	0.04	0.06	0.08	0.096
7	Low vegetation	0.025	0.0375	0.05	0.06
8	River banks (cobble and gravel)	0.0223	0.0341	0.0731	0.08772
9	Bare land with low vegetation	0.03	0.035	0.05	0.06
10	Cobble with low vegetation in some places	0.0318	0.042	0.0878	0.10536
11	* Continuous urban fabric	0.06	0.09	0.12	0.12
12	Discontinuous urban fabric	0.03	0.04	0.05	0.06
13	* Road and rail networks and associated land	0.013	0.013	0.013	0.013
14	Green urban areas	0.017	0.025	0.033	0.0396
15	Non-irrigated arable land	0.025	0.035	0.045	0.054
16	* Olive groves	0.06	0.08	0.1	0.1
17	Light brush and trees	0.035	0.05	0.06	0.072

* Classes that do not change from high to debris due to the already high value or because the category remains unchanged for all scenarios.

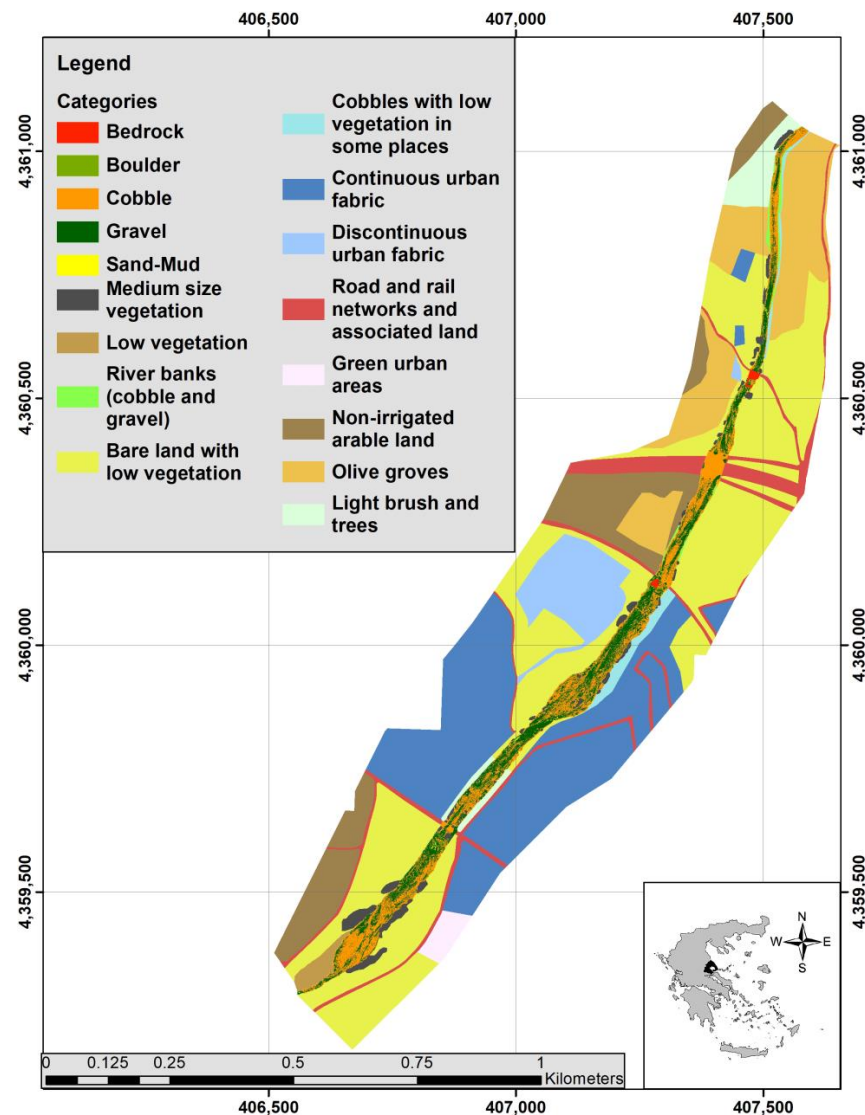


Figure 9. Spatial distribution of Manning’s n roughness coefficient classes.

3.3. Hydraulic Simulation Results

Figure 10 presents the F1 and F2 scores for all possible combinations. From the two examined sensitivity factors (roughness coefficient and modeling approach), the most important one is the roughness coefficient (Figure 10) (F1 varies from 0.31 to 0.716 and F2 varies from -0.281 to 0.664). This finding shows that the methodology followed to determine roughness coefficient values can be very important in flood modeling and mapping efficiency. As expected, the two-dimensional model prevailed among the other modeling approaches with small differences against the coupled (1D/2D) one. On the other hand, one-dimensional modeling approaches provided acceptable solutions relatively close to the other two modeling approaches. An important finding revealed from Figure 10 is that the higher roughness coefficient values provided better results according to F1 and F2 skill scores. Moreover, by considering both validation criteria, we can see that all modeling approaches provided acceptable solutions for the high and debris roughness coefficient scenarios. Finally, the comparison of the F1 and F2 values retrieved from the fifth roughness coefficient scenario against the high roughness coefficient scenario showed that both scores concerning the fifth scenario are approximately lower by 3.6% and 9% from the high scenario, respectively (Figure 10).

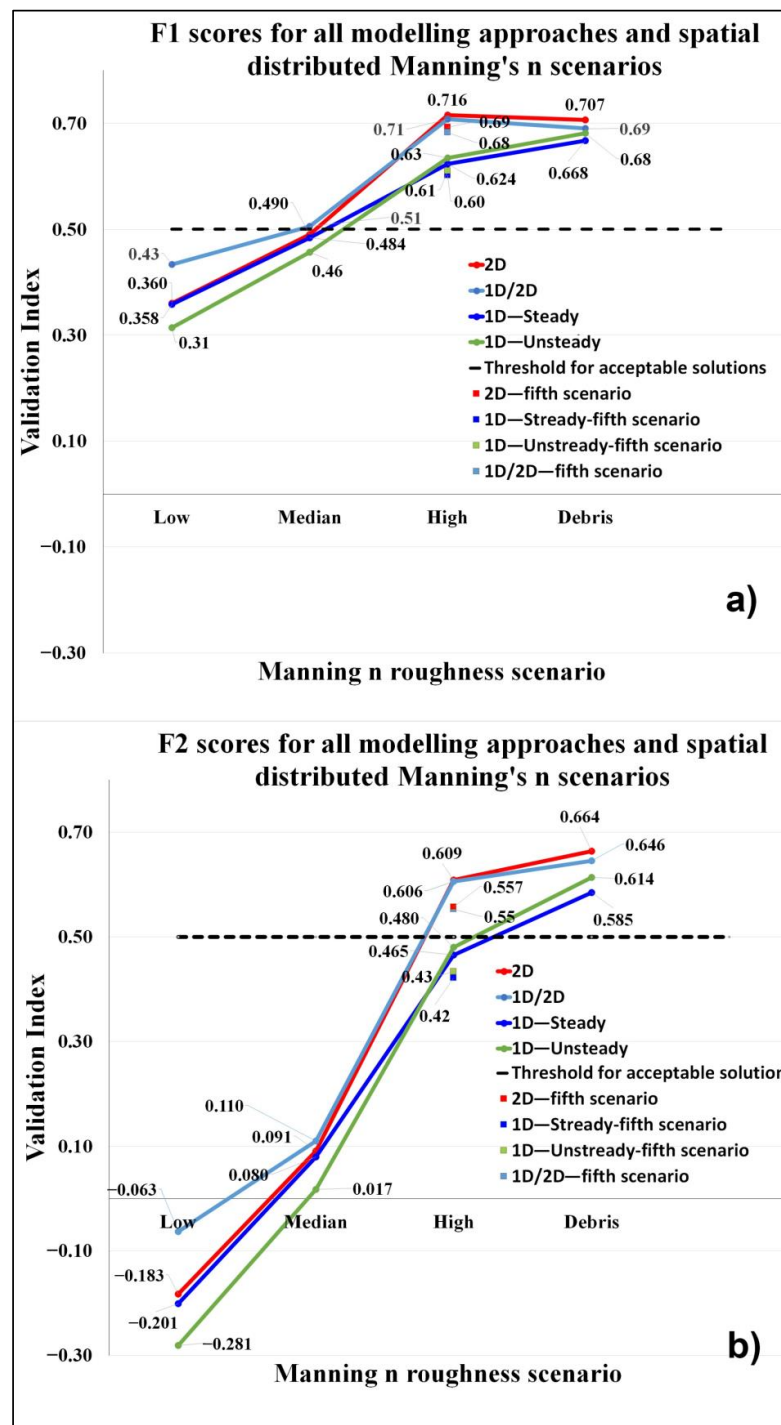


Figure 10. Graph with values of the validation indices F1 and F2 for all examined scenarios and modeling approaches: (a) F1 scores, (b) F2 scores.

Figure 11 presents the optimum solutions of simulated maximum water depth and flood extent based on F1 scores. Finally, both 1D modeling approaches, steady and unsteady state simulations, receive the highest F1 score using the debris roughness scenario (0.668 and 0.682, respectively) and the highest F2 score using the debris roughness scenario (0.585 and 0.614, respectively). Concerning the 2D modeling approach and the coupled modeling approach, the highest F1 score is observed when using the high roughness scenario (0.716 and 0.708, respectively), and the highest F2 score is observed when using the debris roughness scenario (0.664 and 0.646, respectively).

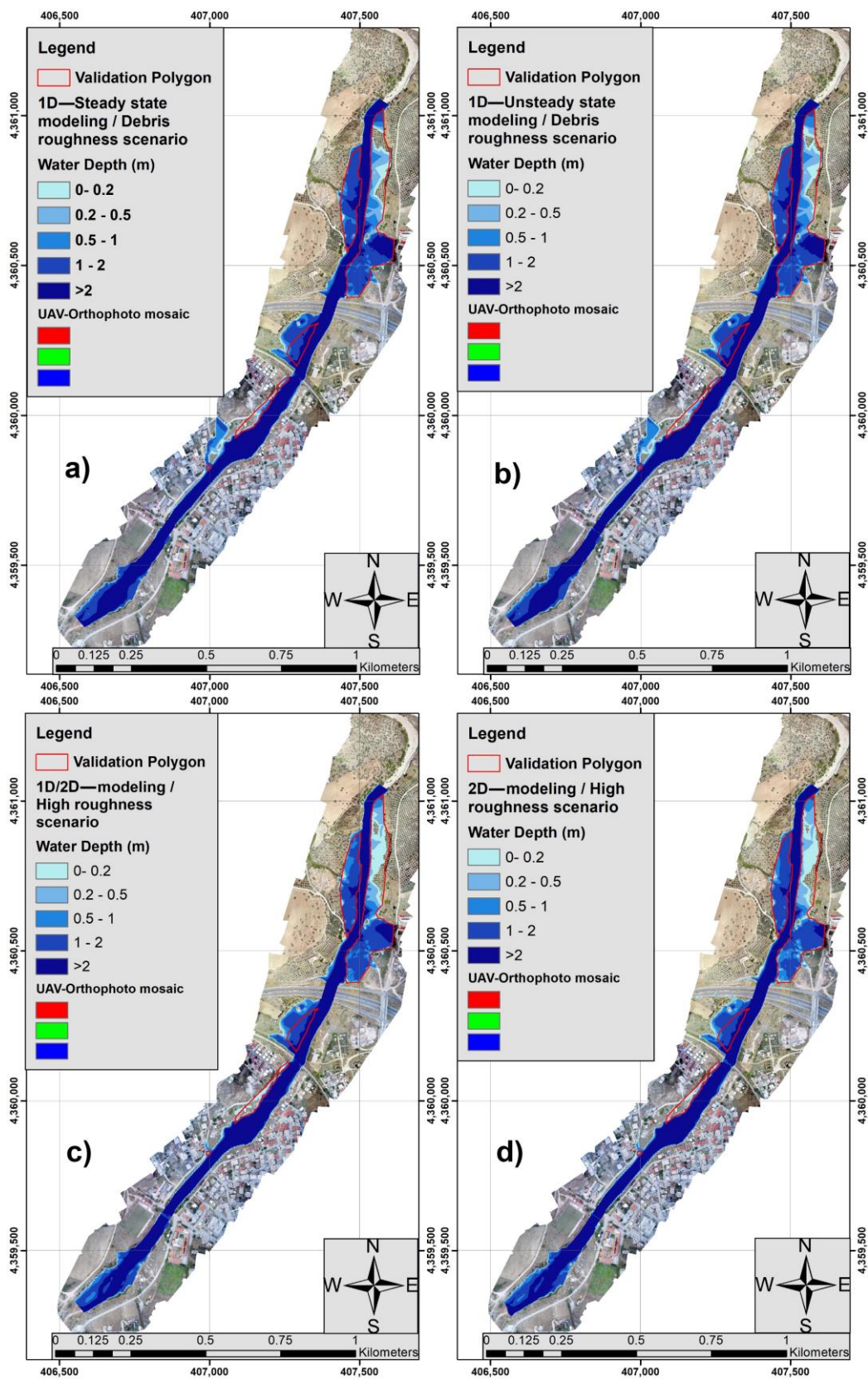


Figure 11. Optimum solutions of simulated maximum water depth and flood extent based on F1 scores: (a) 1D—steady-state modeling approach using debris roughness scenario; (b) 1D—unsteady state modeling approach using debris roughness scenario; (c) Coupled (1D/2D) modeling approach using high roughness scenario; (d) 2D—modeling approach using high roughness scenario.

4. Discussion

In this study, two methods were evaluated for the semi-automated classification of dominant sediment size along the lower part of Xerias stream based on UAV high-resolution data: the first method applied pixel-based and the second OBIA classifications, which implemented texture measures. This research highlighted the segmentation through OBIA as the most effective method of grain size analysis, whereas pixel-based methods presented resolution limitations. According to classification results, the Xerias river bed consists of mixed gravel (50.5%) and cobble (45.7%) bed material with sharp edges, whereas most relevant studies are applied in the different river reach types with more homogeneous compositions [84]. The hereby classification results are in accordance with those derived by several researchers [21,85–87] who reported that OBIA is superior to pixel-based technique, especially for high and very high spatial resolutions, as in our case. The most controversial zones where pixel-based analysis was proven inferior were those dominated by fine sand fractions. On the other hand, it should be noted that those fractions were sufficiently detected by the herein developed hybrid classification method since it employed images with a spatial resolution of a few square centimeters and sufficient image texture [25]. Reclassified microstructure entropy values yielded classification accuracy of approximately 65%, a value similar to other studies [14], which applied GLCM for segmentation-based classification of the dominant substrate in a river bed. Regarding the performance of the classification method based on image texture from the point of view of particles' size, Arif et al. [14] reported that although the accuracy of the algorithm increases with increasing grain size, it resulted in a higher number of misclassified regions for larger grain sizes such as the class of boulders. Respectively, in our case, entropy values managed to estimate a function of the grain sizes, particularly of cobble, gravel and sand-mud classes but not of boulder and bedrock classes. Carbonneau and Lane [25] delineated as the main explanation for not succeeding a higher classification accuracy illumination pattern that can occur as a result of changes in daylight or camera exposure times. Some other widespread fundamental sources of errors hindering greater classification accuracy rates, which were also detected in this study, are the hiding effect of neighboring particles with overlapping classes, the presence of light-dark contact zones created by particles and their shadow, and the high computational capacity that is required when images with the great spatial resolution are elaborated.

The second part of this study presented a subjective way to determine Manning's n roughness values while exploring how the changes in those values may affect the flood extent. Usually, river bed roughness is measured from a small area; the measured value is regarded as the average roughness and is assumed as spatially homogeneous, while a uniform roughness coefficient is determined per river channel and floodplain category [41,66,67,69,88–90]. Few studies in flood inundation modeling, such as Dimitriadis et al. [40], Sharma and Regonda [91], and Papaioannou et al., [36,42], have examined the usage of variable roughness coefficient values, but the channel roughness values were assumed spatially homogeneous. Even fewer works in flood inundation modeling have examined the usage of variable spatial distributed roughness coefficient values for the river bed (e.g., [92]). It should be mentioned that based on F1 and F2 skill scores, the high roughness coefficient scenario provided slightly higher values than the fifth roughness coefficient scenario. This is probably due to the heavy sediment transport processes and even debris flow that occurred during the specific flood event. Concerning the results of this study, the high and debris roughness coefficient scenarios provided the best solutions based on F1 and F2 skill scores. This is probably related to the fact that the topography of the river bed and riverine area is complex because usually, the water in extreme flash flood events is affected by heavy sediment transport processes. The determination of roughness coefficient for an entire stream reach and large areas still remains a demanding process [66,69,88–90], and that is the gap that this study attempted to fill [66,69,88–90]. Especially at ungauged catchments, the implementation of flood inundation modeling and mapping is still a difficult but very important task [30,41,68].

5. Conclusions

Based on this research, it was demonstrated that reliable grain size estimations of a stream reach with inhomogeneous gravel and cobble dominated bed composition can be obtained from digital airborne imagery, provided that image resolution and ground truth grain size measurements are in a fine scale, to capture the actual particle sizes. If properly adjusted, the methods presented in this study allow for semi-automated mapping of at least a smaller grain size (sand-mud, cobble, gravel) with an error of $\pm 35\%$ at a spatial resolution of 1.3 cm.

Furthermore, the evidence from this study indicates that based on the skill scores F1 and F2, the uncertainty induced by the roughness coefficient dominates against the modeling approach. The higher roughness coefficient values provided better approximations of the flood extent. Moreover, the spatially distributed roughness coefficient provided a more accurate model output in relation to the single roughness coefficient. According to the modeling approach selection, this study supports using the 2D modeling approach for ungauged gravel and cobble bed-dominated streams. The overall results also proved that sensitivity analysis should be mandatory in flood modeling and mapping. The proposed methodological approach presented in this study, combining remote sensing and flood modeling, could be a valuable tool for river flood risk management also in other gravel and cobble bed streams (hydrological basins) with similar terrain complexity and hydrological conditions.

Author Contributions: Investigation, G.P., V.M. and E.D.; Conceptualization, G.P. and A.L.; methodology, G.P.; software, G.P. and V.M.; data curation, G.P. and V.M.; Visualization, G.P. and V.M.; writing—original draft preparation, G.P. and V.M.; writing—review and editing, G.P., V.M., E.D. and A.L.; supervision, E.D. and A.L.; funding acquisition, G.P., V.M., E.D. and A.L. All authors have read and agreed to the published version of the manuscript.

Funding: This research is co-financed by Greece and the European Union (European Social Fund-ESF) through the Operational Programme «Human Resources Development, Education and Lifelong Learning 2014–2020» in the context of the project “Remote sensing methodology for roughness estimation in ungauged streams and sensitivity analysis of floods using different hydraulic/hydrodynamic modeling approaches (1D,2D,1D/2D)” (MIS 5048553).

Data Availability Statement: Not applicable.

Conflicts of Interest: The authors declare no conflict of interest.

References

1. Middleton, G.V.; Southard, J.B. *Mechanics of Sediment Movement*; SEPM (Society for Sedimentary Geology): Tulsa, OK, USA, 1984; ISBN 978-1-56576-232-9.
2. Wiberg, P.L.; Dungan Smith, J. Calculations of the Critical Shear Stress for Motion of Uniform and Heterogeneous Sediments. *Water Resour. Res.* **1987**, *23*, 1471–1480. [[CrossRef](#)]
3. John, C.K.; Pu, J.H.; Pandey, M.; Hanmaiahgari, P.R. Sediment Deposition within Rainwater: Case Study Comparison of Four Different Sites in Ikorodu, Nigeria. *Fluids* **2021**, *6*, 124. [[CrossRef](#)]
4. Clifford, N.J.; Robert, A.; Richards, K.S. Estimation of Flow Resistance IN Gravel-Bedded Rivers: A Physical Explanation of the Multiplier of Roughness Length. *Earth Surf. Processes Landf.* **1992**, *17*, 111–126. [[CrossRef](#)]
5. Bray, D.I.; Davar, K.S. Resistance to Flow in Gravel-Bed Rivers. *Can. J. Civ. Eng.* **1987**, *14*, 77–86. [[CrossRef](#)]
6. Pu, J.H.; Wallwork, J.T.; Khan, M.A.; Pandey, M.; Pourshahbaz, H.; Satyanaga, A.; Hanmaiahgari, P.R.; Gough, T. Flood Suspended Sediment Transport: Combined Modelling from Dilute to Hyper-Concentrated Flow. *Water* **2021**, *13*, 379. [[CrossRef](#)]
7. Rice, S.; Church, M. Grain Size along Two Gravel-Bed Rivers: Statistical Variation, Spatial Pattern and Sedimentary Links. *Earth Surf. Processes Landf.* **1998**, *23*, 345–363. [[CrossRef](#)]
8. Bunte, K.; Abt, S.R. *Sampling Surface and Subsurface Particle-Size Distributions in Wadable Gravel-and Cobble-Bed Streams for Analyses in Sediment Transport, Hydraulics, and Streambed Monitoring*; US Department of Agriculture, Forest Service, Rocky Mountain Research Station: Fort Collins, CO, USA, 2001.
9. Wolman, M.G. A Method of Sampling Coarse River-Bed Material. *Trans. Am. Geophys. Union* **1954**, *35*, 951. [[CrossRef](#)]
10. Hey, R.D.; Thorne, C.R. Accuracy of Surface Samples from Gravel Bed Material. *J. Hydraul. Eng.* **1983**, *109*, 842–851. [[CrossRef](#)]
11. Laronne, J.B.; Shlomi, Y. Depositional Character and Preservation Potential of Coarse-Grained Sediments Deposited by Flood Events in Hyper-Arid Braided Channels in the Rift Valley, Arava, Israel. *Sediment. Geol.* **2007**, *195*, 21–37. [[CrossRef](#)]

12. Rice, S.P.; Haschenburger, J.K. A Hybrid Method for Size Characterization of Coarse Subsurface Fluvial Sediments. *Earth Surf. Processes Landf.* **2004**, *29*, 373–389. [[CrossRef](#)]
13. Verdu, J.M.; Batalla, R.J.; Martínez-Casasnovas, J.A. High resolution grain-size characterization of gravel bars using image analysis and geo-statistics. *Geomorphology* **2005**, *72*, 73–93. [[CrossRef](#)]
14. Arif, M.S.M.; Gülch, E.; Tuhtan, J.A.; Thumser, P.; Haas, C. An Investigation of Image Processing Techniques for Substrate Classification Based on Dominant Grain Size Using RGB Images from UAV. *Int. J. Remote Sens.* **2017**, *38*, 2639–2661. [[CrossRef](#)]
15. Chang, F.J.; Chung, C.H. Estimation of Riverbed Grain-Size Distribution Using Image-Processing Techniques. *J. Hydrol.* **2012**, *440–441*, 102–112. [[CrossRef](#)]
16. Sime, L.C.; Ferguson, R.I. Information on Grain Sizes in Gravel-Bed Rivers by Automated Image Analysis. *J. Sediment. Res.* **2003**, *73*, 630–636. [[CrossRef](#)]
17. Graham, D.J.; Reid, I.; Rice, S.P. Automated Sizing of Coarse-Grained Sediments: Image-Processing Procedures. *Math. Geol.* **2005**, *37*, 1–28. [[CrossRef](#)]
18. Graham, D.J.; Rice, S.P.; Reid, I. A Transferable Method for the Automated Grain Sizing of River Gravels. *Water Resour. Res.* **2005**, *41*, 1–12. [[CrossRef](#)]
19. Buscombe, D. Estimation of Grain-Size Distributions and Associated Parameters from Digital Images of Sediment. *Sediment. Geol.* **2008**, *210*, 1–10. [[CrossRef](#)]
20. Beggan, C.; Hamilton, C.W. New Image Processing Software for Analyzing Object Size-Frequency Distributions, Geometry, Orientation, and Spatial Distribution. *Comput. Geosci.* **2010**, *36*, 539–549. [[CrossRef](#)]
21. Sibaruddin, H.I.; Shafri, H.Z.M.; Pradhan, B.; Haron, N.A. Comparison of Pixel-Based and Object-Based Image Classification Techniques in Extracting Information from UAV Imagery Data. In *IOP Conference Series: Earth and Environmental Science*; Institute of Physics Publishing: Bristol, UK, 2018; Volume 169.
22. Haralick, R.M.; Shanmugam, K.; Dinstein, I. Textural Features for Image Classification. *IEEE Trans. Syst. Man Cybern.* **1973**, *SMC-3*, 610–621. [[CrossRef](#)]
23. Connors, R.W.; Trivedi, M.M.; Harlow, C.A. Segmentation of a High-Resolution Urban Scene Using Texture Operators. *Comput. Vis. Graph. Image Processing* **1984**, *25*, 273–310. [[CrossRef](#)]
24. Hawlick, R.M. Statistical and Structural Approaches to Texture. *Proc. IEEE* **1979**, *67*, 786–804.
25. Carbonneau, P.E.; Lane, S.N.; Bergeron, N.E. Catchment-Scale Mapping of Surface Grain Size in Gravel Bed Rivers Using Airborne Digital Imagery. *Water Resour. Res.* **2004**, *40*. [[CrossRef](#)]
26. Apel, H.; Thieken, A.H.; Merz, B.; Blöschl, G. Flood Risk Assessment and Associated Uncertainty. *Nat. Hazards Earth Syst. Sci.* **2004**, *4*, 295–308. [[CrossRef](#)]
27. Papaioannou, G.; Vasiliades, L.; Loukas, A.; Aronica, G.T. Probabilistic Flood Inundation Mapping at Ungauged Streams Due to Roughness Coefficient Uncertainty in Hydraulic Modelling. *Adv. Geosci.* **2017**, *44*, 23–34. [[CrossRef](#)]
28. Coon, W. *Estimation of Roughness Coefficients for Natural Stream Channels with Vegetated Banks*; US Geological Survey: Denver, CO, USA, 1998.
29. Marcus, W.A.; Roberts, K.; Harvey, L.; Tackman, G. An Evaluation of Methods for Estimating Manning's n in Small Mountain Streams. *Mt. Res. Dev.* **1992**, *12*, 227. [[CrossRef](#)]
30. Papaioannou, G. *Flood Hazard and Risk Modelling Framework for Ungauged Streams and Watersheds*; University of Thessaly: Volos, Greece, 2017.
31. Pappenberger, F.; Beven, K.; Horritt, M.; Blazkova, S. Uncertainty in the Calibration of Effective Roughness Parameters in HEC-RAS Using Inundation and Downstream Level Observations. *J. Hydrol.* **2005**, *302*, 46–69. [[CrossRef](#)]
32. Teng, J.; Jakeman, A.J.; Vaze, J.; Croke, B.F.W.; Dutta, D.; Kim, S. Flood Inundation Modelling: A Review of Methods, Recent Advances and Uncertainty Analysis. *Environ. Model. Softw.* **2017**, *90*, 201–216. [[CrossRef](#)]
33. Hutanu, E.; Miha-Pintilie, A.; Urzica, A.; Paveluc, L.E.; Stoleriu, C.C.; Grozavu, A. Using 1D HEC-RAS Modeling and LiDAR Data to Improve Flood Hazard Maps Accuracy: A Case Study from Jijia Floodplain (NE Romania). *Water* **2020**, *12*, 1624. [[CrossRef](#)]
34. Albo-Salih, H.; Mays, L. Testing of an Optimization-Simulation Model for Real-Time Flood Operation of River-Reservoir Systems. *Water* **2021**, *13*, 1207. [[CrossRef](#)]
35. Costabile, P.; Macchione, F. Enhancing River Model Set-up for 2-D Dynamic Flood Modelling. *Environ. Model. Softw.* **2015**, *67*, 89–107. [[CrossRef](#)]
36. Papaioannou, G.; Vasiliades, L.; Loukas, A.; Alamanos, A.; Efstratiadis, A.; Koukouvinos, A.; Tsoukalas, I.; Kossieris, P. A Flood Inundation Modeling Approach for Urban and Rural Areas in Lake and Large-Scale River Basins. *Water* **2021**, *13*, 1264. [[CrossRef](#)]
37. Naem, B.; Azmat, M.; Tao, H.; Ahmad, S.; Khattak, M.; Haider, S.; Ahmad, S.; Khero, Z.; Goodell, C. Flood Hazard Assessment for the Tori Levee Breach of the Indus River Basin, Pakistan. *Water* **2021**, *13*, 604. [[CrossRef](#)]
38. Apel, H.; Aronica, G.T.; Kreibich, H.; Thieken, A.H. Flood Risk Analyses—How Detailed Do We Need to Be? *Nat. Hazards* **2009**, *49*, 79–98. [[CrossRef](#)]
39. Liu, Q.; Qin, Y.; Zhang, Y.; Li, Z. A Coupled 1D–2D Hydrodynamic Model for Flood Simulation in Flood Detention Basin. *Nat. Hazards* **2015**, *75*, 1303–1325. [[CrossRef](#)]
40. Dimitriadis, P.; Tegos, A.; Oikonomou, A.; Pagana, V.; Koukouvinos, A.; Mamassis, N.; Koutsoyiannis, D.; Efstratiadis, A. Comparative Evaluation of 1D and Quasi-2D Hydraulic Models Based on Benchmark and Real-World Applications for Uncertainty Assessment in Flood Mapping. *J. Hydrol.* **2016**, *534*, 478–492. [[CrossRef](#)]

41. Papaioannou, G.; Loukas, A.; Vasiliades, L.; Aronica, G.T. Flood Inundation Mapping Sensitivity to Riverine Spatial Resolution and Modelling Approach. *Nat. Hazards* **2016**, *83*, 117–132. [[CrossRef](#)]
42. Papaioannou, G.; Efstratiadis, A.; Vasiliades, L.; Loukas, A.; Papalexioiu, S.; Koukouvinos, A.; Tsoukalas, I.; Kossieris, P. An Operational Method for Flood Directive Implementation in Ungauged Urban Areas. *Hydrology* **2018**, *5*, 24. [[CrossRef](#)]
43. Chang, C.H.; Chen, H.; Guo, W.D.; Yeh, S.H.; Chen, W.B.; Liu, C.H.; Lee, S.C. Predicting River Embankment Failure Caused by Toe Scour Considering 1D and 2D Hydraulic Models: A Case Study of Da-An River, Taiwan. *Water* **2020**, *12*, 1026. [[CrossRef](#)]
44. Papaioannou, G.; Vasiliades, L.; Loukas, A. Multi-Criteria Analysis Framework for Potential Flood Prone Areas Mapping. *Water Resour. Manag.* **2015**, *29*, 399–418. [[CrossRef](#)]
45. Papaioannou, G.; Varlas, G.; Terti, G.; Papadopoulos, A.; Loukas, A.; Panagopoulos, Y.; Dimitriou, E. Flood Inundation Mapping at Ungauged Basins Using Coupled Hydrometeorological-Hydraulic Modelling: The Catastrophic Case of the 2006 Flash Flood in Volos City, Greece. *Water* **2019**, *11*, 2328. [[CrossRef](#)]
46. Unger, M.; Pock, T.; Grabner, M.; Klaus, A.; Bischof, H. A Variational Approach to Semiautomatic Generation of Digital Terrain Models. In *Proceedings of the Advances in Visual Computing*; Bebis, G., Boyle, R., Parvin, B., Koracin, D., Kuno, Y., Wang, J., Pajarola, R., Lindstrom, P., Hinkenjann, A., Encarnação, M.L., et al., Eds.; Springer: Berlin/Heidelberg, Germany, 2009; pp. 1119–1130.
47. Küng, O.; Strecha, C.; Beyeler, A.; Zufferey, J.-C.; Floreano, D.; Fua, P.; Gervais, F. The Accuracy of Automatic Photogrammetric Techniques on Ultra-Light Uav Imagery. *Int. Arch. Photogramm. Remote Sens. Spat. Inf. Sci.* **2012**, *XXXVIII-1/C22*, 125–130. [[CrossRef](#)]
48. Yuzyk, T.R.; Winkler, T. *Procedures for Bed-Material Sampling: Lesson Package No. 28*; The Section: Ottawa, ON, Canada, 1999; Volume 4.
49. Tuceryan, M.; Jain, A.K. Texture Analysis. In *Handbook of Pattern Recognition and Computer Vision*; World Scientific: Singapore, 1993; pp. 235–276.
50. Ricard, Y.; Bercovici, D. A Continuum Theory of Grain Size Evolution and Damage. *J. Geophys. Res. Solid Earth* **2009**, *114*. [[CrossRef](#)]
51. Markogianni, V.; Dimitriou, E. Landuse and NDVI Change Analysis of Sperchios River Basin (Greece) with Different Spatial Resolution Sensor Data by Landsat/MSS/TM and OLI. *Desalination Water Treat.* **2016**, *57*, 29092–29103. [[CrossRef](#)]
52. Chow, W. *Open-Channel Hydraulics*, 1st ed.; McGraw-Hill: New York, NY, USA, 1959.
53. Brunner, G.W. *CEIWR-HEC. HEC-RAS River Analysis System: 2D Modelling User's Manual Version 6.0*; US Army Corps of Engineers, Hydrologic Engineering Center: Davis, CA, USA, 2021.
54. Phillips, J.; Tadayan, S. *Selection of Manning's Roughness Coefficient for Natural and Constructed Vegetated and Non-Vegetated Channels, and Vegetation Maintenance Plan Guidelines for Vegetated Channels in Central Arizona*; US Geological Survey: Reston, WV, USA, 2007.
55. Hellenic Ministry of Environment and Energy. *1st Update of River Basin Management Plans of the River Basins of Thessaly Water District (EL08). Analysis of the Anthropogenic Pressures and Their Effect on the Surface and Groundwater Waterbodies*; Hellenic Ministry of Environment and Energy, Special Secretariat for Water: Athens, Greece, 2017.
56. McKay, S.K.; Fischenich, J.C. *Robust Prediction of Hydraulic Roughness*; U.S. Army Corps of Engineers (USACE), Coastal and Hydraulics Laboratory: Vicksburg, MS, USA, 2011.
57. Javan, M.; McKeogh, E.; Kiely, G. Field Evaluation of Manning's n in Gravel Rivers. In *Channel Flow Resistance: Centennial of Manning's Formula*; Yen, B., Ed.; Water Resources Publications: Littleton, Hongkong, 1992; pp. 318–327.
58. Ho, C.W.; Huang, H.P. Manning's Roughness Coefficient of Mountainous Streams in Taiwan. In *Channel Flow Resistance: Centennial of Manning's Formula*; Yen, B.C., Ed.; Water Resources Publications: Littleton, Hong Kong, 1992; pp. 299–308.
59. Arcement, G.J.; Schneider, V.R. *Guide for Selecting Manning's Roughness Coefficients for Natural Channels and Flood Plains*; U.S. G.P.O.: Denver, CO, USA, 1984.
60. Romero, M.; Revollo, N.; Molina, J. Flow Resistance in Steep Mountain Rivers in Bolivia. *J. Hydrodyn.* **2010**, *22*, 679–684. [[CrossRef](#)]
61. Ugarte, A.S.; Madrid-Aris, M. Roughness Coefficient in Mountain River. In *Hydraulic Engineering '94*; Cotroneo, G.V., Rumer, R., Eds.; American Society of Civil Engineers: New York, NY, USA, 1994; Volume 1, pp. 652–656.
62. Dey, S.; Saksena, S.; Merwade, V. Assessing the Effect of Different Bathymetric Models on Hydraulic Simulation of Rivers in Data Sparse Regions. *J. Hydrol.* **2019**, *575*, 838–851. [[CrossRef](#)]
63. Gain, A.K.; Mojtabed, V.; Biscaro, C.; Balbi, S.; Giupponi, C. An Integrated Approach of Flood Risk Assessment in the Eastern Part of Dhaka City. *Nat. Hazards* **2015**, *79*, 1499–1530. [[CrossRef](#)]
64. Künzler, M.; Huggel, C.; Ramírez, J.M. A Risk Analysis for Floods and Lahars: Case Study in the Cordillera Central of Colombia. *Nat. Hazards* **2012**, *64*, 767–796. [[CrossRef](#)]
65. Kastridis, A.; Stathis, D. Evaluation of Hydrological and Hydraulic Models Applied in Typical Mediterranean Ungauged Watersheds Using Post-Flash-Flood Measurements. *Hydrology* **2020**, *7*, 12. [[CrossRef](#)]
66. Costabile, P.; Costanzo, C.; Ferraro, D.; Macchione, F.; Petaccia, G. Performances of the New HEC-RAS Version 5 for 2-D Hydrodynamic-Based Rainfall-Runoff Simulations at Basin Scale: Comparison with a State-of-the Art Model. *Water* **2020**, *12*, 2326. [[CrossRef](#)]
67. Czuba, J.A.; David, S.R.; Edmonds, D.A.; Ward, A.S. Dynamics of Surface-Water Connectivity in a Low-Gradient Meandering River Floodplain. *Water Resour. Res.* **2019**, *55*, 1849–1870. [[CrossRef](#)]
68. Papaioannou, G.; Varlas, G.; Papadopoulos, A.; Loukas, A.; Katsafados, P.; Dimitriou, E. Investigating Sea-State Effects on Flash Flood Hydrograph and Inundation Forecasting. *Hydrol. Processes* **2021**, *35*, 1–20. [[CrossRef](#)]

69. Pilotti, M.; Milanese, L.; Bacchi, V.; Tomirotti, M.; Maranzoni, A. Dam-Break Wave Propagation in Alpine Valley with HEC-RAS 2D: Experimental Cancano Test Case. *J. Hydraul. Eng.* **2020**, *146*, 05020003. [[CrossRef](#)]
70. Zhang, K.; Shalehy, M.H.; Ezaz, G.T.; Chakraborty, A.; Mohib, K.M.; Liu, L. An Integrated Flood Risk Assessment Approach Based on Coupled Hydrological-Hydraulic Modeling and Bottom-up Hazard Vulnerability Analysis. *Environ. Model. Softw.* **2022**, *148*, 105279. [[CrossRef](#)]
71. Albo-Salih, H.; Mays, L.W.; Che, D. Application of an Optimization/Simulation Model for the Real-Time Flood Operation of River-Reservoir Systems with One-and Two-Dimensional Unsteady Flow Modeling. *Water* **2022**, *14*, 87. [[CrossRef](#)]
72. Dasallas, L.; Kim, Y.; An, H. Case Study of HEC-RAS 1D–2D Coupling Simulation: 2002 Baeksan Flood Event in Korea. *Water* **2019**, *11*, 2048. [[CrossRef](#)]
73. Brunner, G.W.; Sanchez, A.; Molls, T.; Parr, D.A. *HEC-RAS Verification and Validation Tests*; US Army Corps of Engineers–Hydrologic Engineering Center: Davis, CA, USA, 2018; pp. 1–154.
74. Brunner, G.W. *CEIWR-HEC HEC-RAS River Analysis System: User's Manual Version 6.0*; US Army Corps of Engineers Institute for Water Resources, HEC, January: Davis, CA, USA, 2021.
75. Papaioannou, G.; Papadaki, C.; Dimitriou, E. Sensitivity of Habitat Hydraulic Model Outputs to DTM and Computational Mesh Resolution. *Ecolhydrology* **2020**, *13*, e2182. [[CrossRef](#)]
76. Papaioannou, G.; Loukas, A.; Georgiadis, C. The Effect of Riverine Terrain Spatial Resolution on Flood Modeling and Mapping. In *First International Conference on Remote Sensing and Geoinformation of the Environment (RSCy2013)*; Hadjimitsis, D.G., Themistocleous, K., Michaelides, S., Papadavid, G., Eds.; SPIE: Bellingham, DC, USA, 2013; Volume 8795, p. 87951H.
77. Schumann, G.; Matgen, P.; Cutler, M.E.J.; Black, A.; Hoffmann, L.; Pfister, L. Comparison of Remotely Sensed Water Stages from LiDAR, Topographic Contours and SRTM. *ISPRS J. Photogramm. Remote Sens.* **2008**, *63*, 283–296. [[CrossRef](#)]
78. Wang, W.; Yang, X.; Yao, T. Evaluation of ASTER GDEM and SRTM and Their Suitability in Hydraulic Modelling of a Glacial Lake Outburst Flood in Southeast Tibet. *Hydrol. Process.* **2012**, *26*, 213–225. [[CrossRef](#)]
79. di Baldassarre, G.; Schumann, G.; Bates, P.D.; Freer, J.E.; Beven, K.J. Flood-Plain Mapping: A Critical Discussion of Deterministic and Probabilistic Approaches. *Hydrol. Sci. J.* **2010**, *55*, 364–376. [[CrossRef](#)]
80. Horritt, M.S.; di Baldassarre, G.; Bates, P.D.; Brath, A. Comparing the Performance of a 2-D Finite Element and a 2-D Finite Volume Model of Floodplain Inundation Using Airborne SAR Imagery. *Hydrol. Process.* **2007**, *21*, 2745–2759. [[CrossRef](#)]
81. Lim, N.J.; Brandt, S.A. Flood Map Boundary Sensitivity Due to Combined Effects of DEM Resolution and Roughness in Relation to Model Performance. *Geomat. Nat. Hazards Risk* **2019**, *10*, 1613–1647. [[CrossRef](#)]
82. Sampson, C.C.; Smith, A.M.; Bates, P.D.; Neal, J.C.; Alfieri, L.; Freer, J.E. A High-Resolution Global Flood Hazard Model. *Water Resour. Res.* **2015**, *51*, 7358–7381. [[CrossRef](#)]
83. Shastry, A.; Durand, M.; Neal, J.; Fernández, A.; Phang, S.C.; Mohr, B.; Jung, H.C.; Kari, S.; Moritz, M.; Mark, B.G.; et al. Small-Scale Anthropogenic Changes Impact Floodplain Hydraulics: Simulating the Effects of Fish Canals on the Logone Floodplain. *J. Hydrol.* **2020**, *588*, 125035. [[CrossRef](#)]
84. Ermilov, A.A.; Baranya, S.; Török, G.T. Image-Based Bed Material Mapping of a Large River. *Water* **2020**, *12*, 916. [[CrossRef](#)]
85. Marangoz, A.M.; Oruç, M.; Karakiş, S.; Şahin, H. Comparison of Pixel-Based and Object-Oriented Classification Using IKONOS Imagery for Automatic Building Extraction—Safranbolu Testfield. In *Proceedings of the 20th ISPRS Congress, Istanbul, Turkey, 12–23 July 2004*.
86. Laliberte, A.S.; Rango, A.; Havstad, K.M.; Paris, J.F.; Beck, R.F.; McNeely, R.; Gonzalez, A.L. Object-Oriented Image Analysis for Mapping Shrub Encroachment from 1937 to 2003 in Southern New Mexico. *Remote Sens. Environ.* **2004**, *93*, 198–210. [[CrossRef](#)]
87. Yu, Q.; Gong, P.; Clinton, N.; Biging, G.; Kelly, M.; Schirokauer, D. Object-Based Detailed Vegetation Classification with Airborne High Spatial Resolution Remote Sensing Imagery. *Photogramm. Eng. Remote Sens.* **2006**, *72*, 799–811. [[CrossRef](#)]
88. de Arruda Gomes, M.M.; de Melo Verçosa, L.F.; Cirilo, J.A. Hydrologic Models Coupled with 2D Hydrodynamic Model for High-Resolution Urban Flood Simulation. *Nat. Hazards* **2021**, *108*, 3121–3157. [[CrossRef](#)]
89. Muthusamy, M.; Casado, M.R.; Butler, D.; Leinster, P. Understanding the Effects of Digital Elevation Model Resolution in Urban Fluvial Flood Modelling. *J. Hydrol.* **2021**, *59*, 126088. [[CrossRef](#)]
90. Kastridis, A.; Kirkenidis, C.; Sapountzis, M. An Integrated Approach of Flash Flood Analysis in Ungauged Mediterranean Watersheds Using Post-Flood Surveys and Unmanned Aerial Vehicles. *Hydrol. Process.* **2020**, *34*, 4920–4939. [[CrossRef](#)]
91. Sharma, V.C.; Regonda, S.K. Two-Dimensional Flood Inundation Modeling in the Godavari River Basin, India—Insights on Model Output Uncertainty. *Water* **2021**, *13*, 191. [[CrossRef](#)]
92. Garrote, J.; González-Jiménez, M.; Guardiola-Albert, C.; Díez-Herrero, A. The Manning's Roughness Coefficient Calibration Method to Improve Flood Hazard Analysis in the Absence of River Bathymetric Data: Application to the Urban Historical Zamora City Centre in Spain. *Appl. Sci.* **2021**, *11*, 9267. [[CrossRef](#)]